Supplementary Information for Presentation: "Deriving mixed layer boundary conditions from ocean transient tracer observations"

Daniel E. Sandborn[1], Mark J. Warner[1], Brendan M. Carter[2], Zachary K. Erickson[3]

1: School of Oceanography, University of Washington, Seattle, WA

2: Cooperative Institute for Climate, Ocean, and Ecosystem Studies, University of Washington, Seattle, WA

3: NOAA Pacific Marine Environmental Laboratory, Seattle, WA

December 11, 2025

This document contains supplementary information prepared to accompany research presented at the December 2025 American Geophysical Union meeting in New Orleans, Louisiana. The material below should be treated as preliminary, meant to support continuing discussion rather than stand as a final research result.

Abstract

Uncertainty in formulating boundary conditions for transient tracers and carbon dioxide is the single largest source of error in transit time distribution (TTD) methods, fundamentally limiting transient tracer applications including ventilation age inference and ocean anthropogenic carbon estimation. We derive a maximum mixed layer boundary condition for chlorofluorocarbons 11 and 12 and sulfur hexafluoride using repeat hydrographic observations. A Markov Chain Monte Carlo deconvolution method was employed to invert a surface boundary age spectrum (Green's function) from observations representing the deep winter mixed layer in outcrops of various isoneutral layers. Convolution of the resulting spectra with atmospheric histories of the transient tracers yielded surface boundary functions expressing tracer surface saturation throughout their histories. Application of these functions to climatologically-defined deep winter mixing outcrops yielded a spatially- and temporally-comprehensive product illustrating the evolving surface expressions of transient gases, and enables the formulation of a single-source surface boundary function for TTD age modeling.

Contents

1 References cited in poster presentation

Values refer to citations given in the accompanying poster presentation.

1. He, Y., Tjiputra, J., Langehaug, H. R., Jeansson, E., Gao, Y., Schwinger, J., & Olsen, A. (2018). A Model-Based Evaluation of the Inverse Gaussian Transit-Time Distribution Method for Inferring Anthropogenic Carbon Storage in the Ocean. Journal of Geophysical Research: Oceans, 123(3), 1777–1800. https://doi.org/10.1002/2017JC013504

2. Haine, T. W. N. (2006). On tracer boundary conditions for geophysical reservoirs: How to find the boundary concentration from a mixed condition. Journal of Geophysical Research: Oceans, 111(C5), 2005JC003215. https://doi.org/10.1029/2005JC003215

3. Orsi, A. H., Smethie, W. M., & Bullister, J. L. (2002). On the total input of Antarctic waters to the deep ocean: A preliminary estimate from chlorofluorocarbon measurements. Journal of Geophysical Research: Oceans, 107(C8). https://doi.org/10.1029/2001JC000976

4. Lauvset, S. K., Lange, N., Tanhua, T., Bittig, H. C., Olsen, A., Kozyr, A., Álvarez, M., Azetsu-Scott, K., Brown, P. J., Carter, B. R., Cotrim Da Cunha, L., Hoppema, M., Humphreys, M. P., Ishii, M., Jeansson, E., Murata, A., Müller, J. D., Pérez, F. F., Schirnick, C., … Key, R. M. (2024). The annual update GLODAPv2.2023: The global interior ocean biogeochemical data product. Earth System Science Data, 16(4), 2047–2072. https://doi.org/10.5194/essd-16-2047-2024

5. Johnson, G. C., & Lyman, J. M. (2022). GOSML: A Global Ocean Surface Mixed Layer Statistical Monthly Climatology: Means, Percentiles, Skewness, and Kurtosis. Journal of Geophysical Research: Oceans, 127(1), e2021JC018219. https://doi.org/10.1029/2021JC018219

6. Cimoli, L., Gebbie, G., Purkey, S. G., & Smethie, W. M. (2023). Annually Resolved Propagation of CFCs and SF6 in the Global Ocean Over Eight Decades. Journal of Geophysical Research: Oceans, 128(3), e2022JC019337. https://doi.org/10.1029/2022JC019337

7. Bullister, J. L., & Warner, M. J. (2017). Atmospheric Histories (1765-2022) for CFC-11, CFC-12, CFC-113, CCl4, SF6 and N2O (NCEI Accession 0164584) [Dataset]. NOAA National Centers for Environmental Information. https://doi.org/10.3334/CDIAC/OTG.CFC_ATM_HIST_2015

8. Meinshausen, M., Nicholls, Z. R. J., Lewis, J., Gidden, M. J., Vogel, E., Freund, M., Beyerle, U., Gessner, C., Nauels, A., Bauer, N., Canadell, J. G., Daniel, J. S., John, A., Krummel, P. B., Luderer, G., Meinshausen, N., Montzka, S. A., Rayner, P. J., Reimann, S., … Wang, R. H. J. (2020). The shared socio-economic pathway (SSP) greenhouse gas concentrations and their extensions to 2500. Geoscientific Model Development, 13(8), 3571–3605. https://doi.org/10.5194/gmd-13-3571-2020

9. Shao, A. E., Mecking, S., Thompson, L., & Sonnerup, R. E. (2013). Mixed layer saturations of CFC-11, CFC-12, and SF6 in a global isopycnal model: Surface Saturation of CFCs and SF6. Journal of Geophysical Research: Oceans, 118(10), 4978–4988. https://doi.org/10.1002/jgrc.20370

10. Raimondi, L., Tanhua, T., Azetsu-Scott, K., Yashayaev, I., & Wallace, D. W. R. (2021). A 30 -Year Time Series of Transient Tracer-Based Estimates of Anthropogenic Carbon in the Central Labrador Sea. Journal of Geophysical Research: Oceans, 126(5), e2020JC017092. https://doi.org/10.1029/2020JC017092

11. Haine, T. W. N., Griffies, S. M., Gebbie, G., & Jiang, W. (2025). A Review of Green's Function Methods for Tracer Timescales and Pathways in Ocean Models. Journal of Advances in Modeling Earth Systems, 17(7), e2024MS004637. https://doi.org/10.1029/2024MS004637

12. Carter, B. R., Schwinger, J., Sonnerup, R., Fassbender, A. J., Sharp, J. D., Dias, L. M., & Sandborn, D. E. (2025). Tracer-based rapid anthropogenic carbon estimation (TRACE). Earth System Science Data, 17(6), 3073–3088. https://doi.org/10.5194/essd-17-3073-2025

13. Sandborn, D.E, Carter, B.R., Warner, M.J., Erickson, Z.K. "TRACE-Python: Tracer-based Rapid Anthropogenic Carbon Estimation Implemented in Python (version 1.0)". In review.

2 Introduction

Hydrographic surveys of chlorofluorocarbons (CFCs) and sulfur hexafluoride (SF_6) have enabled detailed illustration of the ocean's ventilation pathways on decadal scales and aided the constraint of ocean circulation state estimates and ocean anthropogenic carbon (C_{anth}) inventories (Erickson et al., 2023). These products rely upon accurately-estimated surface boundaries for age tracers in order to resolve water mass ages and circulation pathways, yet observation-based spatially- and temporally-resolved surface boundaries for CFCs and SF_6 have proved elusive due to data sparsity and the nature of water mass formation (Wunsch, 2002; Li & Wunsch, 2004).

The conditions of formation of subducted waters are fleeting, interannually-variable, and therefore difficult to observe in situ. Subducted waters tend to be highly biased by season, with preformed tracer concentrations set by the conditions of deepest winter mixing in a phenomenon that has come to be known as "Stommel's Demon" [1] by which a "demon" lets only the densest, coldest parcels of water subduct (Stommel, 1979). This metaphor has been explored in a variety of modeling and observational studies and found to generally represent the reality of age tracer boundary condition well, despite simplifying the nature of tracer transport (Williams et al., 1995). An attempt to describe the "selection" of water parcels to form the surface boundary must then rely upon continuous monitoring to observe the moment of selection and the contemporaneous tracer concentrations, model this phenomenon using parameterized tracer fluxes, or infer it from measurements at other places and times. This work adopts the latter strategy upon consideration of the strengths and weaknesses of the other options.

Transient tracer surface boundaries have been estimated by global ocean circulation models, which demonstrated profound seasonal variability in mixed layer transient tracer saturation in many regions. Shao et al. (2013) and Rodehacke et al. (2010) used circulation model simulation of CFC transport to illustrate this variability on a global and regional scale, respectively, finding lag in deep winter mixed layer saturation versus the atmosphere created by some combination of seasonal thermal variability, brief deep convective mixing periods relative to equilibration timescales, seasonal ice cover, and mixing with old relatively tracer-depleted waters. Winter undersaturation of CFCs relative to the atmosphere was amplified at high latitudes, but difficult to ground-truth due to sparse measurement. Such modeling studies benefit from spatiotemporally-comprehensive results, but suffer from high sensitivity to modeled parameterization of air-sea

[1] In reference to Maxwell.

gas flux and complex mixed layer circulation among other phenomena, which may introduce error into their output.

An alternative strategy of inferring a surface boundary condition from observations circumvents the need to specify gas flux or mixing parameterizations, but must overcome sparse observation. In recognition of the role of lag in mixed layer tracer equilibration with the atmosphere, recent work gave surface boundaries for CFCs, SF_6 and radiocarbon as functions of their atmospheric histories inferred by inversion from observations (DeVries & Primeau, 2010; Cimoli et al., 2023). The present work takes a similar approach, with a focus on refining techniques for statistical inversion of single-source surface boundaries from mixed layer observations by Bayesian deconvolution with minimal prior guidance. We further examine the drivers and consequences of these inverted surface boundaries as new and interesting descriptions of surface ocean circulation in their own right. First the forward problem is described to clarify the relationship of transient tracer saturation drivers, then the inverse problem is described to set the stage for a statistical inversion.

2.1 Forward Problem

The transit time distribution (TTD) method propagates a boundary condition through the ocean by means of a boundary propagator function $\mathcal{G}$, which can be expressed as a Green's function solution of the linear advection diffusion equations. $\mathcal{G}$ may be derived from ocean circulation model output or inferred from tracer observations under a variety of frameworks such as the inverse-gaussian solution of the advection diffusion equations for one-dimensional pipe flow (Hall et al., 2002). The tracer concentration χ given by the TTD method is solved as a convolution of the surface boundary concentration χ_s with the boundary propagator expressed at time t, for location r, and lag time t':

$$\chi(r,t) = \int_0^\infty \chi_s(t')\mathcal{G}(r,t;t-t')dt' \tag{1}$$

Propagated tracer fields depend upon an accurate formulation of the surface boundary for skillful application. Formally, the surface boundary must be expressed as a Dirichlet boundary condition, yet for tracers including trace gases such as CFCs and SF_6, surface concentration depends upon the rate of air-sea gas flux, leading to the physical reality of these tracers as subject to a Robin or mixed condition, which complicates their role in the TTD framework considerably (Haine, 2006). The task of converting the mixed boundary condition of trace gases to a concentration or Dirichlet condition may be simplified by assuming perfect air-sea equilibrium for one or more tracers (Waugh et al., 2006), or

by assuming a fractional saturation with respect to the atmosphere (Waugh et al., 2004), each incurring some error. Haine (2006) generalized the expression of a (space- and time-varying) surface boundary concentration condition as a function of the varying atmospheric condition (χ_{atm}) with a second convolution integral:

$$\chi_s(r,t') = \int_0^\infty \chi_{atm}(t'')\mathcal{K}(r,t';t'-t'')dt'dt'' \tag{2}$$

in which $\mathcal{K}$ is a kernel expressing the contribution of past atmospheric conditions to χ_s at lag time t'. The case of perfect atmospheric equilibrium for a given tracer can be expressed in this framework by replacing the convolution kernel with the Dirac delta function. $\mathcal{K}$ [2] may be determined from circulation model output or some simple analytical circulation schema (Haine, 2006) or inverted from observations assumed to represent the boundary (DeVries & Primeau, 2010; Cimoli et al., 2023). It is the latter inversion method which this study seeks to improve and apply to transient tracers.

2.2 Inverse Problem

The inverse problem of solving Equation 2 for $\mathcal{K}(r,t')$ (hereafter: the surface age spectrum) relies on first identifying observations representing χ_s from hydrographic time series, then solving for an age spectrum of unknown shape. This problem must be regularized to account for spatial variability in surface saturation drivers, which we accomplish by considering a set of outcrops of isoneutral layer outcrops defined by neutral density. This strategy simplifies the inference of the proper surface boundary for a deep water mass by reference to neutral density as a function of salinity, temperature, and geographic coordinates (Jackett & McDougall, 1997). The inversion also makes the assumption of steady state circulation in order to isolate the spatially-varying behavior of tracer saturation.

At the heart of the statistical inversion technique described in this work is a Bayesian approach to deconvolution which attempts to make as few prior assumptions of the behavior of the surface age spectrum as possible in the interest of obtaining an honest description of its value as dictated by observations and their variability. In setting up an inversion without strong functional prior, this work aims to develop a clearer theory of the relationship of observed surface age spectrum with both the drivers of transient tracer transport and provide a

[2] Variously: the boundary condition kernel, equilibrium time distribution, surface Green's function kernel, others.

useful empirical product to inform continuing transient tracer-based ocean state estimation.

3 Data and Methods

Transient tracer observations from the GLODAPv2.2023 data product were selected to give observations most closely approximating conditions of the relict winter deep mixed layer, then used to constrain transient tracer age spectra and surface boundaries for a range of isoneutral layer outcrops. GLODAP observations of transient tracers were subset to include only bottles shallower than the maximum mixed layer (MML) at cast locations, defined as the median value of the depth of the mixed layer in the month with the greatest such median value in the GOSML mixed layer gridded monthly climatology (Johnson & Lyman, 2022). Within the MML, transient tracer observations were again subset as in Cimoli et al. (2023) by selecting the tracer measurements from each cast for each of CFC-11, CFC-12, and SF_6 with the largest concentration. These samples were expected to most closely represent conditions of the relict deep winter mixed layer by merit of being formed in conditions of minimum temperature and therefore highest solubility. It is also assumed these conservative species' concentrations are minimally biased by sub-annual variability from e.g. air-sea gas flux and diffusive transport, being sequestered shallower than the MML depth and deeper than the mixed layer observed contemporaneously. Temperature and salinity of the MML conditions from the GOSML climatology were used to convert transient tracer measurements given in molar amount per mass of seawater to mixing fractions (i.e. units of parts-per-trillion, ppt) using the solubility functions of Warner and Weiss (1985) and Bullister et al. (2002), assuming that error in assuming an atmospheric pressure of 1 atm would be negligible in aggregate. Later conversion of surface boundaries expressed as mixing fractions to boundaries expressed as molal concentrations proceeded by the same process in reverse. Similarly, each observation was assigned a neutral density (γ^n) calculated from MML conditions from the GOSML climatology. Climatological median temperature, salinity, and γ^nvalues from GOSML were utilized in order to avoid bias from subsurface warming and stratification that would accompany in-situ values obtained during periods not associated with deep winter mixing.

The resulting time series of transient tracer observations spanned more than four decades. Recasting them as air-sea disequilibria with respect to contemporaneously-observed mean global atmospheric mixing fractions (Bullister & Warner, 2017) indicated undersaturation on a global scale largely obscured

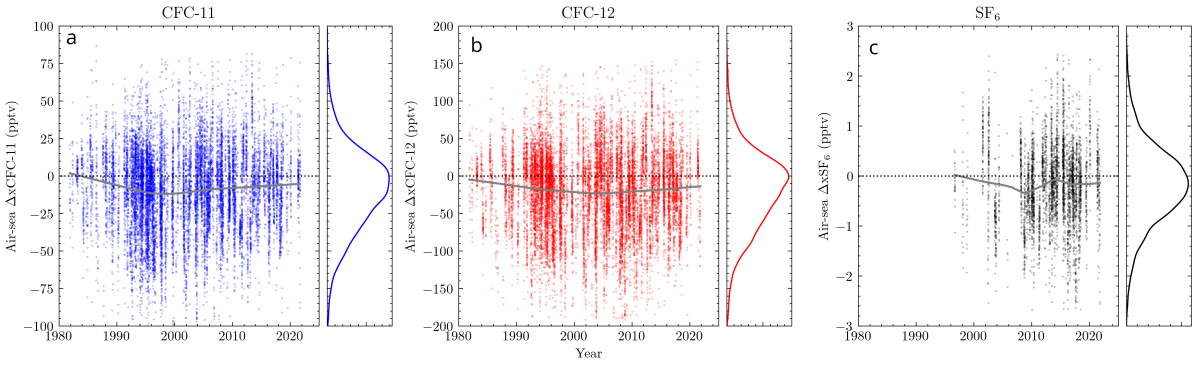

Figure 1: Time series of transient tracer observations from the GLODAPv2.2023 data product subset to give those most closely approximating conditions of deep winter mixing and subduction and transformed to indicate atmospheric disequilibrium by subtracting the global mean atmospheric mixing fraction from transient tracer observations. Positive values indicate observed supersaturation, while negative values indicate undersaturation. LOESS regressions are plotted as grey lines for each transient tracer to indicate overall time series trends. Kernel density estimations are plotted to the right of each time series, indicating a general pattern of undersaturation over the observed histories. **a, b.** CFC-11 and CFC-12 observations show increasing air-sea disequilibrium until c. 2000 c.e. as expected from the Transient Steady State Assumption, followed by declining disequilibrium. **c.** SF_6 observations display an uncertain trend over time due to apparently sparse data shifted by outliers.

by relatively larger variability around a moving-average mean (Figure 1). This variability was resolved by spatial regularization of the inverse problem followed by statistical inversion propagating variability into uncertainty around transient tracer surface boundaries.

Regularization of the inverse problem proceeded by spatial subsetting among outcrops of approximately neutral surfaces defined by ranges of γ^n. For each isoneutral layer γ^n_i in the set [24.0, 24.5, 25.0, ..., 27.0, 27.2, 27.4, ..., 27.75, 27.8, 27.85, ..., 28.1] all observations with a (GOSML climatology-assigned) γ^n between γ^n_{i-1} and γ^n_{i+1} were grouped together for inversion, resulting in a "moving window" scheme. Observations outside this range were assigned to the nearest value, as too few existed to constrain further outcrops. Further subsetting by ocean basin proved difficult, as highly uneven observation density (Fig. 2) prevented reliable deconvolution in sparsely-observed regions, though hemispheric subsetting remains an option for future work.

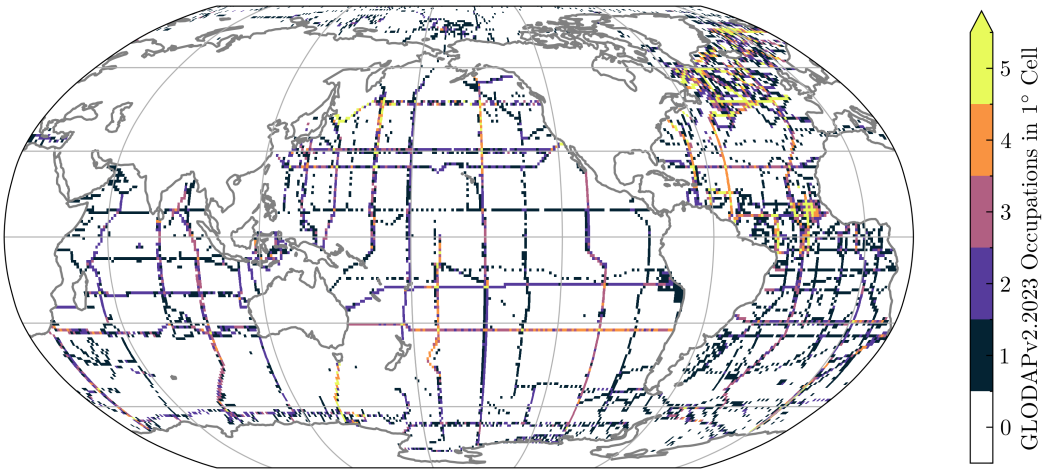

Figure 2: Occupations in the GLODAPv2.2023 product, grouped by 1-degree latitude and longitude cell. An occupation was defined as the number of months of occurrences of transect data in a cell in order to avoid counting simultaneous or continuous/frequent reoccupations.

3.1 Deconvolution Approach

For each of i isoneutral layer outcrops r_i, deconvolution of the transient tracer age spectrum $\mathcal{K}(r_i; t')$ began by defining a basis for t' (also known as a support) of 25 years, which was found to accommodate at least 99.9% of the area of all deconvoluted $\mathcal{K}(r, t')$. Minimally-informative priors for $\mathcal{K}(r, t')$ were constructed by defining 150 discrete points arranged at two-month intervals along the basis and constraining the range and sum of the set of discrete points to realistic values using a Dirichlet distribution. A Markov Chain Monte Carlo deconvolution was prepared to iteratively improve the set of $\mathcal{K}(r, t')$ by comparing their convolutions with the age histories of the transient tracers against observations for each of i outcrops as selected in Section 3. The sampling process was carried out using the "No U-Turn" sampling algorithm and Monte Carlo framework provided by the PyMC package (Abril-Pla et al., 2023).

Initial tests of the deconvolution found that CFC-11 and CFC-12 observation time series individually constrained satisfactory age spectra, yet the SF_6 data were unable to constrain surface age spectra converging on stable behaviors for reasons likely including large measurement relative uncertainty, spatial binning error, inter-cruise bias, and the lack of an observed atmospheric roll-off. This latter characteristic was found necessary to unambiguously define age spectra,

as CFC-11 and CFC-12 data restricted to before their respective atmospheric roll-off dates produced similarly unconstrained age spectra likely as a result of unresolved covariance among discrete points of their surface age spectra. To overcome this barrier to creating a surface boundary for SF_6, a deconvolution was formulated which constrained age spectra for all three transient tracers after adjusting for their varying solubility and air-sea gas exchange characteristics.

This joint deconvolution rested on the assumption that for identical mixed layer physical environments, gas exchange equilibration timescales were responsible for all observed differences in tracer disequilibrium with respect to the atmosphere. $\mathcal{K}(t')$ may be understood as a decay timescale specifying the declining relative influence of the value of $\chi_{atm}(t)$ over lag time t'. The rate of decay is largely controlled by the timescale of the slowest-decaying component, and Haine (2006) demonstrated that for CFCs in a diffusive mixed layer on the scale of tens to hundreds of meters (most of the global ocean except deep water formation regions) the timescale of equilibration with an overlying atmosphere is controlled by air-sea gas flux rather than physical diffusion or chemical equilibration. For this reason we suggest that $\mathcal{K}$ deconvoluted from the behavior of one conservative and passive tracer can be scaled to approximate the $\mathcal{K}$ expected for a second similar tracer by the ratio of the two tracers' characteristic equilibration times.

The characteristic equilibration time τ_e for a tracer in a mixed layer undergoing air-sea gas exchange is given as a function of the mixed layer depth z_m and the piston velocity of the tracer k_w (Broecker & Peng, 1982):

$$\tau_e = \frac{z_m}{k_w} \tag{3}$$

For identical mixed layers (or sufficiently-similar mixed layers grouped spatially), the mean ratio of characteristic air-sea equilibration timescales for two tracers "a" and "b" may then be expressed as the inverse ratio of their piston velocities:

$$\frac{\tau_{e,a}}{\tau_{e,b}} = \frac{k_{w,b}}{k_{w,a}} \tag{4}$$

Once again assuming identical mixed layers, Equation 2 may be recast as a function of their Schmidt numbers (Watson et al., 1991):

$$\frac{\tau_{e,a}}{\tau_{e,b}} = \left(\frac{Sc_{w,b}}{Sc_{w,a}}\right)^{0.5} \tag{5}$$

which were calculated from each outcrop's climatological winter deep mixing temperature and salinity using the parameterizations of Wanninkhof (2014).

For the case of the CFCs this ratio was very nearly unity within the range of oceanic conditions. In contrast, the ratio of equilibration times for SF_6 versus CFC-11 was around 93% at 20 °C and salinity 35, such that the characteristic air-sea equilibration time for SF_6 was expected to be approximately 7% faster. This ratio was utilized to scale the surface age spectra constrained by CFCs and apply it to SF_6.

In this way, CFC-11 and CFC-12 observations jointly constrained surface age spectra by scaling $\mathcal{K}$ linearly in the t' dimension by the ratio of the characteristic air-sea equilibration timescales of the two tracers, then normalizing $\mathcal{K}$ to retain the original area under the curve. Co-constraint using a Markov Chain Monte Carlo approach to optimize its fit and estimate error allowed this deconvolution to overcome sparse data availability and deconvolute age spectra for isoneutral slab outcrops between γ^n = 24 – 28.1 kg m^{-3}. An example of the deconvolution process for a single isopycnal layer outcrop (Figure 3) demonstrates the result. The solution of the inverse problem produced a posterior surface age spectrum $\mathcal{K}(t')$ optimized such that its convolution with transient tracer atmospheric histories produced a surface boundary χ_s capturing the magnitude and temporal trend of observations while incorporating their misfit into propagated uncertainty (Section 3.3). The validity of this method was supported by its comparable reconstruction of surface boundaries for CFCs and SF_6, the latter of which was not used to constrain the deconvolution (Section 4.2).

3.2 Convolution of surface boundaries

Transient tracer surface boundaries were produced from surface age spectra by substituting $\mathcal{K}(r, t')$ into Equation 2 and integrating to produce $\chi_s(r, t)$, a set of surface boundaries spanning the industrial period for various discrete γ^n outcrops. These were recast into saturation with respect to the atmosphere by calculating percent saturation (r_sat) as

$$r_{sat} = \frac{\chi_s(t)}{\chi_{atm}(t)} \times 100\% \tag{6}$$

The use of the set of $\mathcal{K}(r, t')$ to produce surface boundaries for an arbitrary isoneutral layer was demonstrated in a two-step process using the GOSML climatology as a globe-spanning example. First, age spectra were collected and interpolated along axes of lag time t' and γ^n using three-dimensional piecewise cubic hermite spline interpolation to produce a surface describing the contribution of atmospheric tracer concentration history at lag time t' as a function of γ^n. Second, the GOSML climatology, subset as before to isolate the conditions of maximum winter mixing, was used to calculate γ^n outcrops. For each cell in the

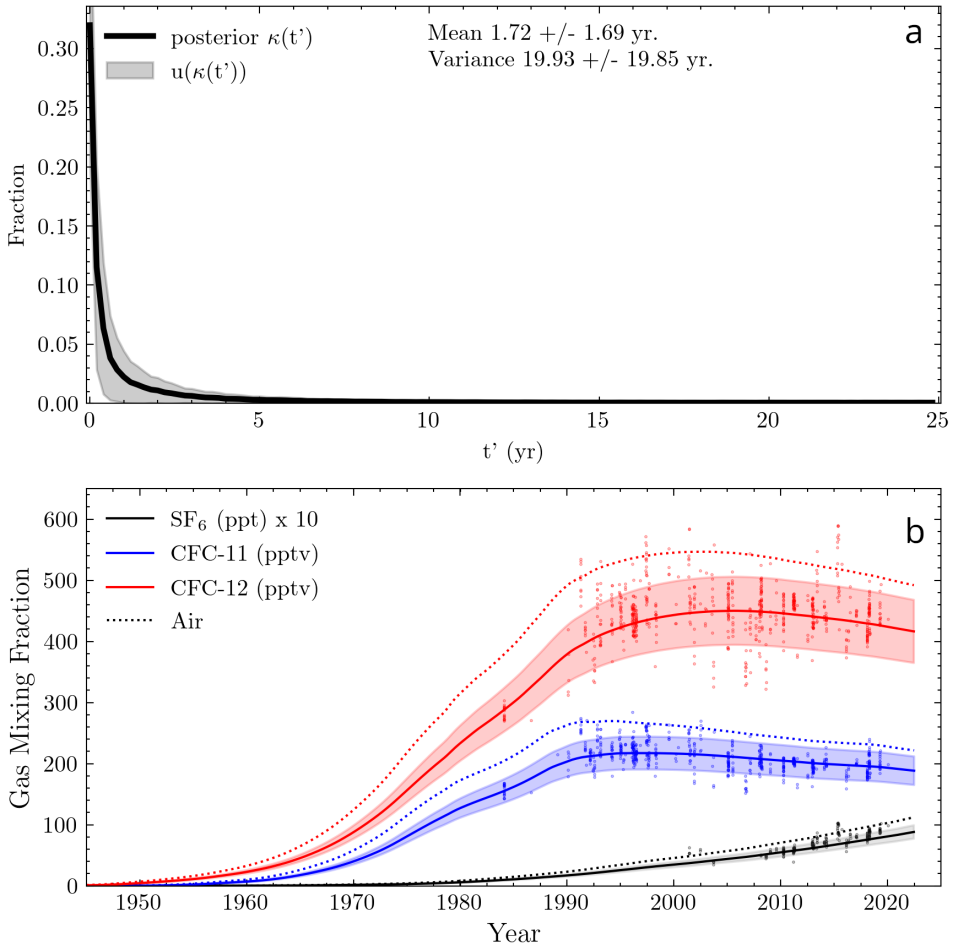

Figure 3: Example deconvolution results for an isopycnal layer outcrop defined by the range of γ^n 26 – 26.5 kg m^{-3}. **a.** Surface age spectrum $\mathcal{K}(t')$ indicating the dominance of atmospheric signals younger than five years in determining transient tracer surface boundary concentrations. The solid line indicates the maximum a posteriori estimate and the shaded range indicates its 68% highest posterior density interval (HPDI). The mean age and variance of $\mathcal{K}(t')$ are given with uncertainties given for the upper and lower HPDI. **b.** Convolution of the surface age spectrum in **a.** with transient tracer atmospheric histories shown as dotted lines to yield surface boundary conditions (shown as solid lines) for CFC-11, CFC-12, and SF_6 in units of parts per trillion (ppt), scaled by a factor of 10x for SF_6. Shaded uncertainties were determined from reconstruction-data misfit (Section 3.3).

climatology, the resulting γ^n was used to slice the age spectrum surface. This interpolated age spectrum was then convoluted with the corresponding northern or southern hemisphere atmospheric history, yielding surface boundaries for CFC-11, CFC-12, and SF_6 spanning the industrial era, together with their uncertainties propagated by the Markov Chain Monte Carlo deconvolution.

3.3 Uncertainty analysis

Uncertainty in $\mathcal{K}(r, t')$ was calculated as an integral part of its Markov Chain Monte Carlo deconvolution. Prior estimated measurement uncertainty was given as 3 % for CFC observations (Stöven et al., 2015), which was used in the Bayesian updating scheme to estimate the probability distribution of the posterior estimate of $\mathcal{K}(r, t')$, given as highest posterior density intervals. Uncertainty was propagated through to χ_s by simulation of bottle samples at the same locations and times of the constraining data, then calculation of root mean square relative error (RMSRE). This latter relative error proved to be much larger than estimated measurement uncertainty due to additional non-prior-estimated contributors to observation variability such as spatial binning error, interannual mixed layer circulation variability, error in selection of bottle samples to represent the winter maximum mixed layer conditions, and cruise-level bias.

Additional evaluation of methodological error and uncertainty may be accomplished by replication of the deconvolution using circulation model output and comparison of the resulting tracer surface boundaries to those which would be given by the tracer concentrations in the winter MML as given by the model. This is left to future work, and for this reason, the uncertainties given with the results below should be considered preliminary.

4 Preliminary Results and Discussion

Repeat hydrographic measurements of CFC-11 and CFC-12 constrained an inversion of surface age spectra which defined the lag in winter deep mixing concentrations of transient tracers in a convolution with their atmospheric histories. The surface age spectra were derived for a selection of isoneutral surface outcrops spanning 24 – 28.1 kg m^{-3}. For each outcrop the corresponding surface age spectrum was convoluted with the atmospheric histories of CFC-11, CFC-12, and SF_6 to give surface boundary functions and associated uncertainties implied by the observations. We interpret the age spectra as concise descriptions of winter mixed layer behaviors which effect transient tracer disequilibria, propose quantitative interpretations of their forms, demonstrate their explanatory rela-

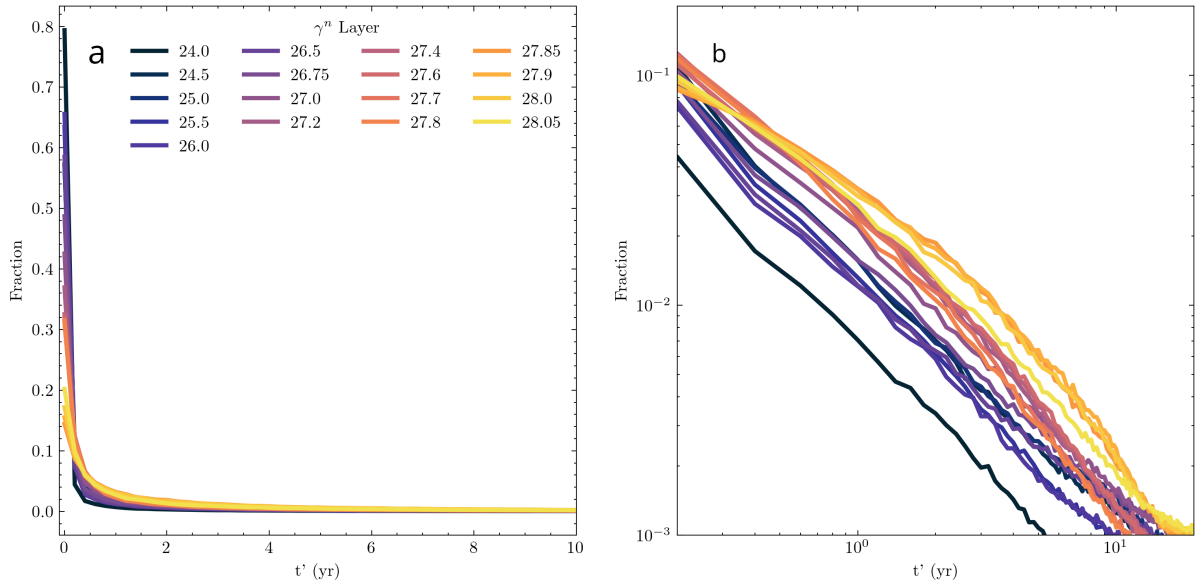

Figure 4: Surface age spectra $\mathcal{K}$ for selected layer outcrops spanning 24 – 28.1 kg m^{-3}. **a.** Linear axes display the controlling influence of recent atmospheric signals in determining MML transient tracer behavior. **b.** A log-log transformation yields generally linear behavior indicative of a power law relationship.

tionship with surface boundary conditions. Finally we outline a framework for applying these results in the context of TTD age modeling along with various next steps to advance this line of research.

4.1 Surface age spectra

Surface age spectra $\mathcal{K}$ produced for a variety of isoneutral layer outcrops illustrate the declining influence of the atmospheric history of a given transient tracer at time t over increasing lag time t'. These spectra (plotted as maximum a posteriori estimates) take the form of an apparently smoothly decaying function across the range of γ^n considered (Figure 4a). High-γ^n outcrops (relative to their lower-γ^n peers) were associated with declining relative contributions of small t' atmospheric signals in favor of large t' atmospheric signals. This trend is maintained across the range of isoneutral layer outcrops given here. For all $\mathcal{K}$, 99% of the area under $\mathcal{K}$ lay under 10 years' lag time t', such that the "memory" of the mixed layer is largely limited to this period.

The consistent shape of $\mathcal{K}$ across isoneutral layers was found with minimal

prior constraints, indicating robustness of the deconvolution in the face of relatively noisy observational histories. Transforming the surface age spectra with log-log axes emphasizes this consistency further, as the decaying functions are found to become generally linear (Figure 4b). Linearity in log-log-transformed functions is a sign of a power law relationship. In the case of the negative log-log slopes illustrated here, an inverse power law functional form may be inferred for the surface age spectra of transient tracers. Future work should seek to interpret this consistent inverse power law form in terms of physical characteristics such as transport dimensionality.

4.2 Transient tracer surface boundaries

Convoluting surface age spectra with the atmospheric histories of CFC-11, CFC-12, and SF_6 yielded reconstructed surface boundaries for each isoneutral slab outcrop (Figure 5). An array of tracer surface boundaries displayed decreasing saturation with respect to the atmosphere at higher γ^n(Figure 6, in qualitative agreement with previous modeled and observation-based products. Undersaturation was observed for all three tracers for the 20th century, while in the 21st century several of the lightest outcrops displayed apparent supersaturation after approximately 2005 for CFC-11 and 2010 for CFC-12. SF_6 remained undersaturated with respect to the atmosphere for all years and locations, uniformly increasing its depth of disequilibrium over the observed period in accordance with the expectations of the transient steady state assumption.

Interpolation of $\mathcal{K}$ for each cell of the GOSML climatology using γ^n calculated from salinity and temperature associated with the period of deepest winter mixing and convolution of the resulting ensemble of surface boundary spectra with the atmospheric histories of the transient tracers gave a spatially- and temporally- comprehensive illustration of the saturation of transient tracers in the winter MML with respect to the atmosphere (Figures 7–10). A broad increase in undersaturation of the CFCs was evident in years leading up to the roll-off after which undersaturation decreased. Deep water-forming regions including the Greenland and Labrador Seas as well as the Antarctic continental margin were marked by the most undersaturated conditions for each gas. Given that the deconvolution method described here is limited to γ^n lighter than approximately 28.1 kg m^{-3}, detailed examination of Antarctic Bottom Water formation transient tracer saturation remains out of reach, but North Atlantic Deep Water formation may serve as a target for future study.

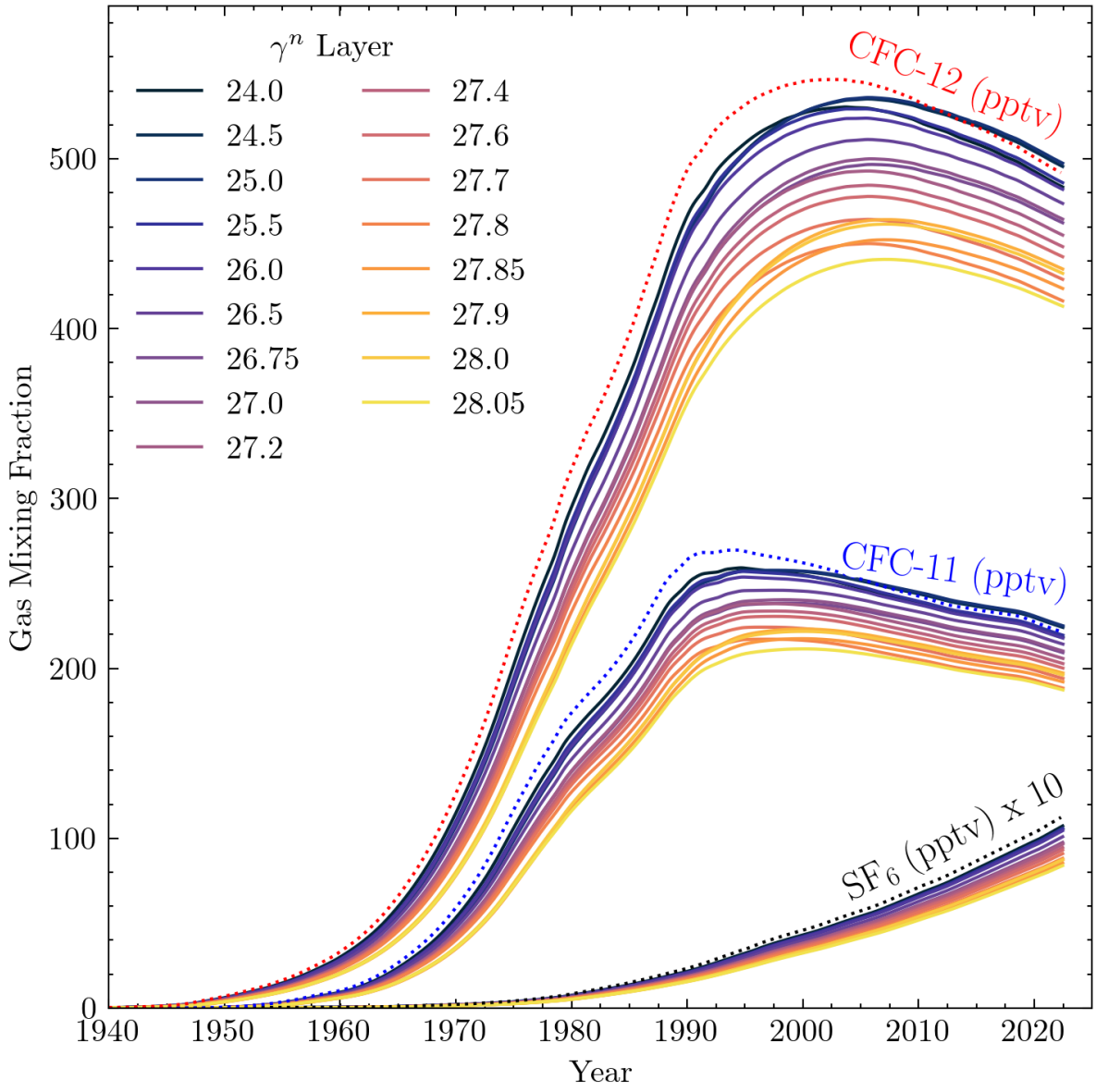

Figure 5: Transient tracer surface boundaries for selected isoneutral layer outcrops defined by γ^ncompared to tracers' atmospheric histories. Boundaries and atmospheric histories are given as mixing fractions in units of parts per trillion (ppt) for CFC-11 and CFC-12, and ppt x 10 for SF_6. Greater vertical distance between surface boundaries and the atmospheric history indicates greater disequilibrium

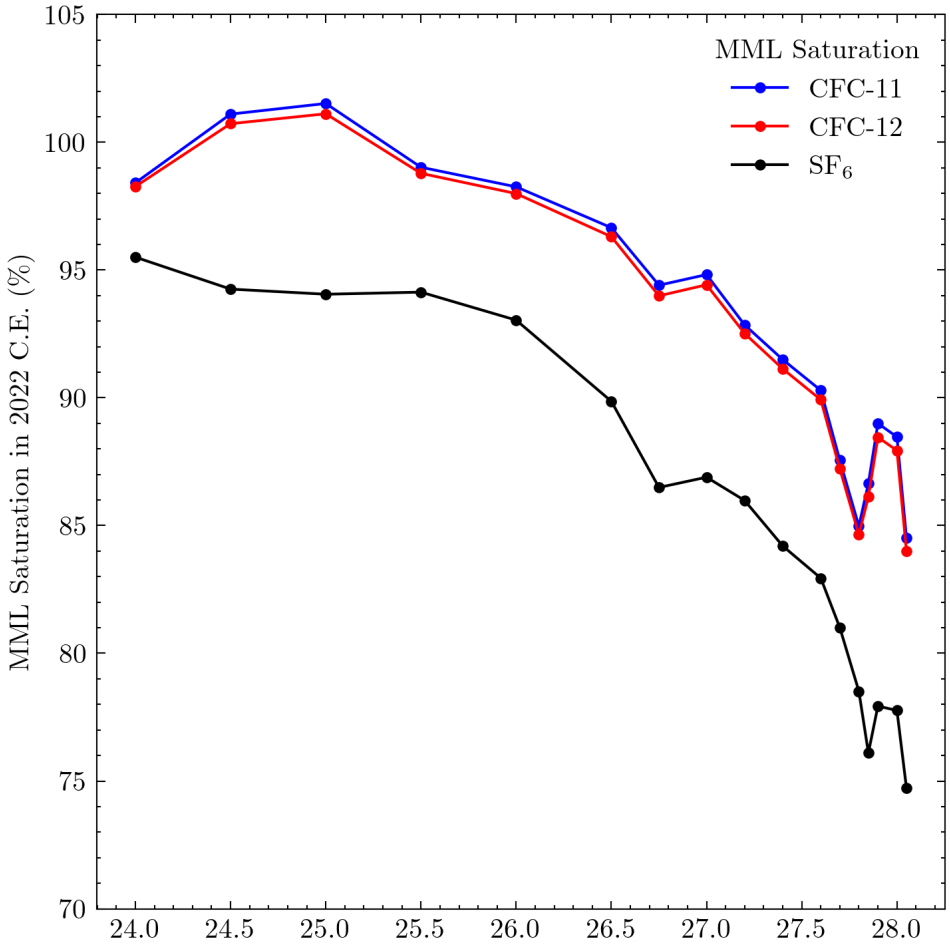

Figure 6: Saturation of transient tracer MML surface boundaries at isoneutral layer outcrops defined by γ^n given for the year 2022 c.e. in terms of percent saturation with respect to the tracers' atmospheric concentrations. A generally-declining trend in saturation was observed with increasing γ^n as expected from previous work.

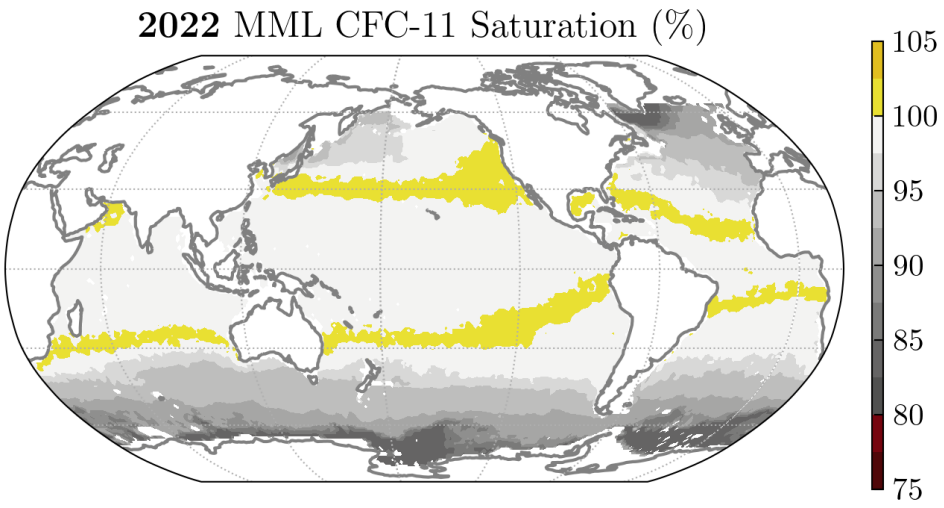

Figure 7: Surface boundary saturation of CFC-11 relative to the atmosphere in 2022 C.E. assuming in-situ salinity and temperature given by maximum mixed layer conditions in the GOSML climatology.

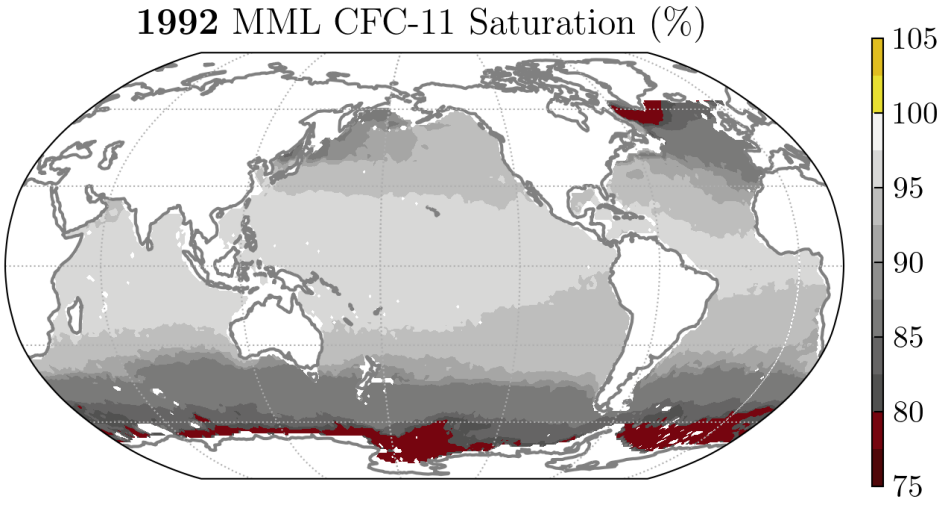

Figure 8: Surface boundary saturation of CFC-11 relative to the atmosphere in 1992 C.E. assuming in-situ salinity and temperature given by maximum mixed layer conditions in the GOSML climatology.

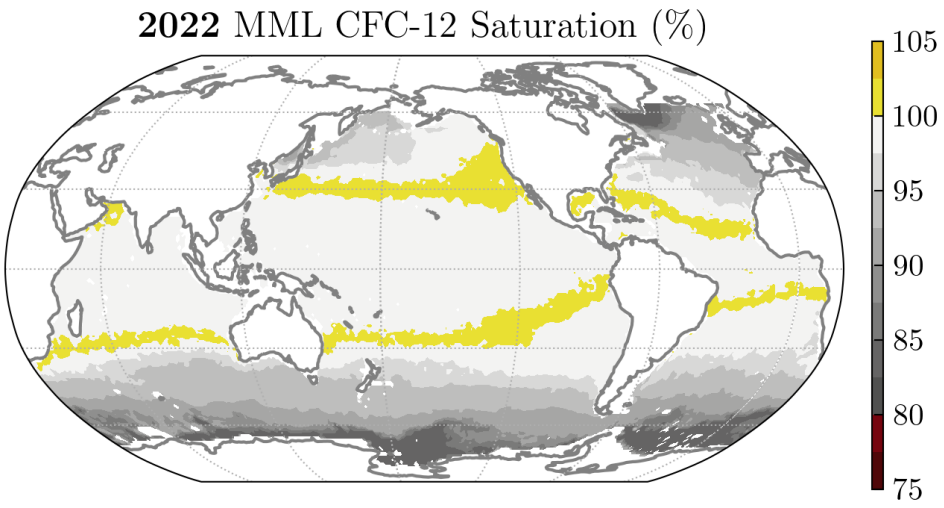

Figure 9: Surface boundary saturation of CFC-12 relative to the atmosphere in 2022 C.E. assuming in-situ salinity and temperature given by maximum mixed layer conditions in the GOSML climatology.

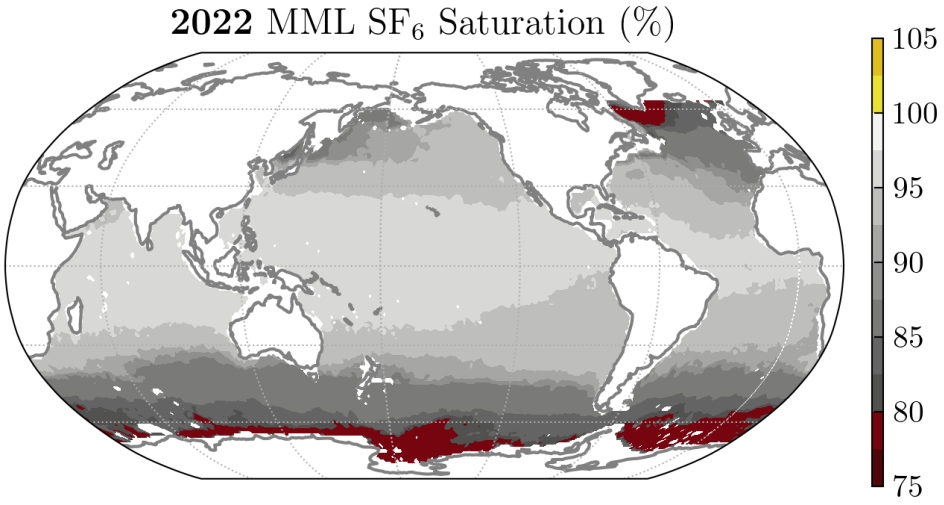

Figure 10: Surface boundary saturation of SF_6 relative to the atmosphere in 2022 C.E. assuming in-situ salinity and temperature given by maximum mixed layer conditions in the GOSML climatology.

4.3 Application to tracer age modeling and anthropogenic carbon estimation

Integration of the surface boundary conditions derived in this study with (single-source) TTD age modeling and anthropogenic carbon estimation may be accomplished by selecting an outcrop of interest, selecting the corresponding surface boundary given by this work (or solving for a new one), and solving Equation 1 for the boundary propagator $\mathcal{G}$ as demonstrated by several recent studies (Carter et al., 2025; Cimoli et al., 2023; Sonnerup et al., 2015). Demonstration of this process is among the next steps in this study, along with defining and propagating an improved observation-based surface boundary condition for anthropogenic carbon.

References

Abril-Pla, O., Andreani, V., Carroll, C., Dong, L., Fonnesbeck, C. J., Kochurov, M., … Zinkov, R. (2023). PyMC: A modern and comprehensive probabilistic programming framework in Python. *PeerJ Computer Science*, *9*(e1516). doi: 10.7717/peerj-cs.1516

Broecker, W. S., & Peng, T.-H. (1982). *Tracers in the Sea*. Lamont-Doherty Earth Observatory, Columbia University.

Bullister, J. L., & Warner, M. J. (2017). *Atmospheric Histories (1765-2022) for CFC-11, CFC-12, CFC-113, CCl4, SF6 and N2O (NCEI Accession 0164584).* NOAA National Centers for Environmental Information. doi: 10.3334/CDIAC/OTG.CFC_ATM_HIST_2015

Bullister, J. L., Wisegarver, D. P., & Menzia, F. A. (2002, January). The solubility of sulfur hexafluoride in water and seawater. *Deep Sea Research Part I: Oceanographic Research Papers*, *49*(1), 175–187. doi: 10.1016/S0967-0637(01)00051-6

Carter, B. R., Schwinger, J., Sonnerup, R., Fassbender, A. J., Sharp, J. D., Dias, L. M., & Sandborn, D. E. (2025). Tracer-based rapid anthropogenic carbon estimation (TRACE). *Earth System Science Data*, *17*(6), 3073–3088. doi: 10.5194/essd-17-3073-2025

Cimoli, L., Gebbie, G., Purkey, S. G., & Smethie, W. M. (2023, March). Annually Resolved Propagation of CFCs and SF_6 in the Global Ocean Over Eight Decades. *JGR Oceans*, *128*(3), e2022JC019337. doi: 10.1029/2022JC019337

DeVries, T., & Primeau, F. (2010, July). An improved method for estimating water-mass ventilation age from radiocarbon data. *Earth and Planetary Science Letters*, *295*(3-4), 367–378. doi: 10.1016/j.epsl.2010.04.011

Erickson, Z., Carter, B., Feely, R., Johnson, G., Sharp, J., & Sonnerup, R. (2023). PMEL's Contribution to Observing and Analyzing Decadal Global Ocean Changes Through Sustained Repeat Hydrography. *Oceanog*. doi: 10.5670/oceanog.2023.204

Haine, T. W. N. (2006, May). On tracer boundary conditions for geophysical reservoirs: How to find the boundary concentration from a mixed condition. *J. Geophys. Res.*, *111*(C5), 2005JC003215. doi: 10.1029/2005JC003215

Hall, T. M., Haine, T. W. N., & Waugh, D. W. (2002, December). Inferring the concentration of anthropogenic carbon in the ocean from tracers. *Global Biogeochemical Cycles*, *16*(4). doi: 10.1029/2001GB001835

Jackett, D. R., & McDougall, T. J. (1997, February). A Neutral Density Variable for the World's Oceans. *J. Phys. Oceanogr.*, *27*(2), 237–263. doi: 10.1175/1520-0485(1997)027<0237:ANDVFT>2.0.CO;2

Johnson, G. C., & Lyman, J. M. (2022, January). GOSML: A Global Ocean Surface Mixed Layer Statistical Monthly Climatology: Means, Percentiles, Skewness, and Kurtosis. *JGR Oceans*, *127*(1), e2021JC018219. doi: 10.1029/2021JC018219

Li, X., & Wunsch, C. (2004, January). An adjoint sensitivity study of chlorofluorocarbons in the North Atlantic. *J. Geophys. Res.*, *109*(C1), 2003JC002014. doi: 10.1029/2003JC002014

Rodehacke, C. B., Roether, W., Hellmer, H. H., & Hall, T. (2010, February). Temporal variations and trends of CFC11 and CFC12 surface-water saturations in Antarctic marginal seas: Results of a regional ocean circulation model. *Deep Sea Research Part I: Oceanographic Research Papers*, *57*(2), 175–198. doi: 10.1016/j.dsr.2009.09.008

Shao, A. E., Mecking, S., Thompson, L., & Sonnerup, R. E. (2013, October). Mixed layer saturations of CFC-11, CFC-12, and SF_6 in a global isopycnal model: Surface Saturation of CFCs and SF_6. *J. Geophys. Res. Oceans*, *118*(10), 4978–4988. doi: 10.1002/jgrc.20370

Sonnerup, R. E., Mecking, S., Bullister, J. L., & Warner, M. J. (2015, May). Transit time distributions and oxygen utilization rates from chlorofluorocarbons and sulfur hexafluoride in the Southeast Pacific Ocean. *JGR Oceans*, *120*(5), 3761–3776. doi: 10.1002/2015JC010781

Stommel, H. (1979, July). Determination of water mass properties of water pumped down from the Ekman layer to the geostrophic flow below. *Proc. Natl. Acad. Sci. U.S.A.*, *76*(7), 3051–3055. doi: 10.1073/pnas.76.7.3051

Stöven, T., Tanhua, T., Hoppema, M., & Bullister, J. L. (2015, September). Perspectives of transient tracer applications and limiting cases. *Ocean Sci.*, *11*(5), 699–718. doi: 10.5194/os-11-699-2015

Wanninkhof, R. (2014, June). Relationship between wind speed and gas exchange over the ocean revisited: Gas exchange and wind speed over the ocean. *Limnol. Oceanogr. Methods*, *12*(6), 351–362. doi: 10.4319/lom.2014.12.351

Warner, M., & Weiss, R. (1985, December). Solubilities of chlorofluorocarbons 11 and 12 in water and seawater. *Deep Sea Research Part A. Oceanographic Research Papers*, *32*(12), 1485–1497. doi: 10.1016/0198-0149(85)90099-8

Watson, A. J., Upstill-Goddard, R. C., & Liss, P. S. (1991, January). Air–sea gas exchange in rough and stormy seas measured by a dual-tracer technique. *Nature*, *349*(6305), 145–147. doi: 10.1038/349145a0

Waugh, D. W., Haine, T. W., & Hall, T. M. (2004, November). Transport times and anthropogenic carbon in the subpolar North Atlantic Ocean. *Deep Sea Research Part I: Oceanographic Research Papers*, *51*(11), 1475–1491. doi: 10.1016/j.dsr.2004.06.011

Waugh, D. W., Hall, T. M., McNeil, B. I., Key, R., & Matear, R. J. (2006, January). Anthropogenic CO_2 in the oceans estimated using transit time distributions. *Tellus B: Chemical and Physical Meteorology*, *58*(5), 376. doi: 10.1111/j.1600-0889.2006.00222.x

Williams, R. G., Marshall, J. C., & Spall, M. A. (1995, December). Does Stommel's Mixed Layer "Demon" Work? *J. Phys. Oceanogr.*, *25*(12), 3089–3102. doi: 10.1175/1520-0485(1995)025<3089:DSMLW>2.0.CO;2

Wunsch, C. (2002, June). Oceanic age and transient tracers: Analytical and numerical solutions. *J. Geophys. Res.*, *107*(C6). doi: 10.1029/2001JC000797